Peer reviewed version

University of Bristol - Explore Bristol Research
General rights

What is the Ultimate Capability of Acoustophoretic Volumetric Displays?

Tatsuki Fushimi,[1, 2, a)] Bruce W. Drinkwater,[2] and Thomas L. Hill[2]

[1)]*Department of Engineering Mathematics, University of Bristol, BS8 1UB, Bristol, United Kingdom*

[2)]*Department of Mechanical Engineering, University of Bristol, BS8 1TR, Bristol, United Kingdom*

(Dated: 19 May 2020)

Advances in acoustophoresis have allowed the recent development of a free-space volumetric display called an Acoustophoretic Volumetric Display (AVD) that can render 3D graphics observable without obstructions. The current generation of AVD can render simple vector graphics in real-time, but larger and complex graphics require 10 seconds or more to render. Here we present a generalized model of an AVD and use this to understand its performance limits; in particular, we answer the question of how large a display (1:1 raster screen) can be created? We show that AVD performance is affected by the size and properties of the particle, along with the viscosity of the surrounding fluid. Optimal performance is achieved when the viscous drag force and inertial force are minimized relative to the acoustic radiation force. Our model suggests that, for expanded polystyrene particles ($\rho_p = 19\,\mathrm{kg\,m^{-3}}$), a screen size of up to 117 mm by 117 mm can be rendered at 10 Hz with an acoustic frequency of 20 kHz, and an acoustic pressure amplitude of 25 kPa.

[a)]Electronic mail: t.fushimi@bristol.ac.uk

There has been a rapid development of volumetric displays that utilize levitated particles in mid-air to render three-dimensional graphics. Smalley et al. developed the optical trap display (OTD) in 2018[1] and Berthelot & Bonod developed an electrically-driven display in 2019[2]. Fushimi et al. demonstrated the feasibility of an acoustophoretic volumetric display (AVD)[3] and Hirayama et al. similarly demonstrated an AVD with multimedia capability in 2019[4]. In all of the examples above, a levitated particle is rapidly moved along a defined trajectory and the graphics are rendered by illuminating the particle (e.g. with an RGB light). The levitated particle reflects the light, and due to the particle's rapid movement, it renders graphics in mid-air through the persistence of the vision effect. These acoustic displays build on a rich history of work in which the acoustic radiation force is used to control objects in various media[5–7].

Whilst the feasibility of a volumetric display using a remotely manipulated particle has been demonstrated, the real-time rendering ability of such a display has been limited to small sizes and simple vector graphics. Larger and more complex graphics e.g. raster displays, in both OTDs and AVDs currently require rendering times of ≥ 10 seconds[1,3,4]. Thus, a natural, but as yet unanswered question is whether it is possible to displace particles at a higher velocity, and therefore render a larger graphical object with higher update frequency?

Here, we address this question and identify the capabilities of an AVD by constructing a relatively simple model that captures the governing physics. The model is based on a nonlinear dynamic model of acoustic levitation[8], and considers 4 forces: acoustic radiation force, inertia, gravity/buoyancy and viscous drag force[9]. In Fushimi et al.[3], it was demonstrated that there are many experimental challenges in the design of AVDs, such as the narrowband transducers, and image deformation caused by static equilibrium point shifts. Our intention here is to look beyond the few current examples of AVDs and explore what might be possible in future devices. We hope this model will assist the future development of AVDs by providing suitable sets of parameters that achieve the best performance for a given objective, such as maximizing the size of rendered images.

We first simplify the problem by describing a generalized AVD that renders its graphics with one spherical particle in mid-air at room temperature (20 °C with density (ρ_0), speed of sound (c_0) and viscosity (μ) assumed to be $1.205 \, \mathrm{kg \, m^{-3}}$, $343.4 \, \mathrm{m \, s^{-1}}$, and $1.813 \times 10^{-5} \, \mathrm{kg \, (m \, s)^{-1}}$, respectively). Whilst the use of multiple particles is of interest for AVDs; each particle is still limited by the same fundamental forces; hence, here we provide insight into the effects of these limitations on the performance of single-particle AVDs. The particle is assumed to have a rigid surface (both

compressional wave speed c_c and shear wave speed $c_s \to \infty$). This rigid particle assumption is thought reasonable for most solid or liquid particles levitated in air as it inherently means c_c, $c_s \gg c_0$. We then simplify the motion of the particle in the generic AVD to be oscillatory and describe the motion in a generalized form:

$$x(t) = A\cos(\omega_p t) \tag{1}$$

$$v(t) = -A\omega_p \sin(\omega_p t) \tag{2}$$

$$a(t) = -A\omega_p^2 \cos(\omega_p t) \tag{3}$$

where x, v and a are displacement, velocity, and accelerations respectively, A is the amplitude of particle motion, and ω_p is the particle frequency. Here, we assume the particle to have a vertical raster format (similarly to methods described by[3]), which allows for numerous display applications, and also simplifies the problem to a single dimension. Horizontal forces are also necessary, however, the performance of the AVD will be limited by its capability to move the particles in the fast vertical direction. We note that graphics may be rendered in numerous other ways: e.g. curved path optimization.

We further assume that, in the local vicinity of the particle, the acoustic field is a 1D plane standing wave of a sinusoidal shape. This allows the evaluation of the AVD without restricting the calculation to a specific set of transducers or arrays. In addition, we note that the sinusoidal pressure function in the vicinity of the acoustic trap is a common assumption in acoustic levitators[8]. The acoustic trap will be moved such that the resultant movement of the particle becomes sinusoidal, as specified in Eq. 1. Methods for calculating the acoustic radiation force (ARF) acting on a spherical particle have been studied by various authors[10–15]. Here, we utilize the formulation by Chen & Apfel to evaluate the amplitude of the ARF[16,17] (F_{rad}): $F_{rad}(\rho_p, r, f_f, p_0) = \left| \frac{\pi p_0^2}{\rho_0 \omega_f^2} K \right|$, where p_0 and $\omega_f = 2\pi f_f$ are pressure amplitude and acoustic angular frequency, respectively and $K = \sum_{m=0}^{\infty}(m+1)(-1)^m(-\beta_m + \beta_{m+1} + 2\alpha_m\beta_{m+1} - 2\beta_m\alpha_{m+1})$ is an infinite sum. The infinite sum was calculated until it converged (relative change $\frac{|K_{n+1}-K_n|}{|K_{n+1}|} < 10^{-10}$), and the comparison of Chen & Apfel to Gor'kov's equations is available in supplementary material. We note that changes in the particle properties can invert the sign of the ARF, which will alter the equilibrium position of the particle; however, the magnitude of the maximum ARF will not be affected. It is assumed that the acoustic pressure amplitude stays constant regardless of the amplitude of the oscillation or location of the acoustic trap and that the transducers can sustain their output even in the cases where the phases of the transducers need to change rapidly[3]. As demonstrated in Fushimi et al.[8], acoustic
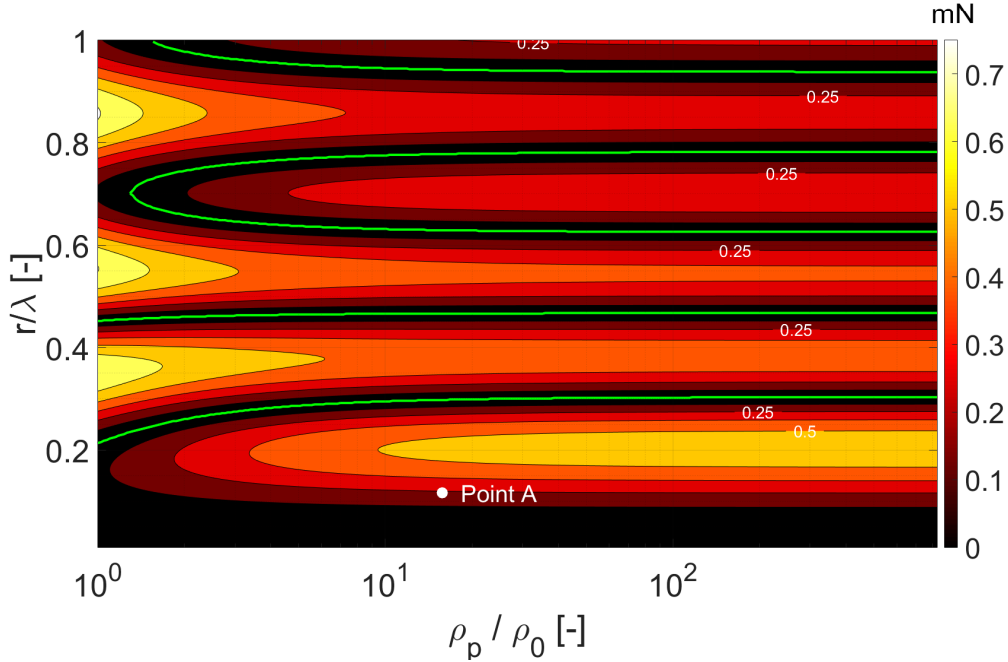
3

FIG. 1: Acoustic radiation force amplitude (F_{rad}) using the formulation of Chen & Apfel[16] when $p_0 = 5\,\text{kPa}$ and $f_f = 40\,\text{kHz}$, as a function of normalized density $\left(\frac{\rho_p}{\rho_0}\right)$ and normalized radius $\left(\frac{r}{\lambda}\right)$. The green line denotes the combinations of density and radius that gives $F_{rad} = 0$.

levitators are rich in nonlinear responses and future AVDs will require advanced control mechanisms to force the particle in the specified trajectory. Further, we assume that the generation time of the acoustic trap is faster than the dynamics of the particle[18,19]. The constants $\alpha_m = \mathbb{R}(B_m)$, $\beta_m = \mathbb{I}(B_m)$, where $B_m = \frac{\iota D_m}{(1 - \iota D_m)}$ and where for a rigid particle[16], $D_m = \frac{\widetilde{\rho} j_m(kr)) - kr \cdot j_m'(kr)}{\widetilde{\rho} n_m(kr)) - kr \cdot n_m'(kr)}$ when $m = 1$, and $D_m = \frac{j_m'(kr)}{n_m'(kr)}$ when $m \neq 1$. $\widetilde{\rho} = \frac{\rho_0}{\rho_p}$, $j_m(x)$ and $n_m(x)$ are the spherical Bessel and Neumann functions of order m and argument x, respectively. We utilize the above ARF equations for a rigid sphere, but the model can easily be changed to accommodate other types of sphere such as fluid, or elastic spheres (all simulation codes utilized in this analysis is available online). The variable r is the radius of the particle and $k = \frac{2\pi f_f}{c_0}$ is the wavenumber. Fig. 1 shows an example of the calculated acoustic radiation force amplitude, using Chen & Apfel, as a function of normalized density ($\frac{\rho_p}{\rho_0}$) and normalized radius ($\frac{r}{\lambda}$ where $\lambda = \frac{c_0}{f_f} = 8.6\,\text{mm}$ for 40 kHz at room temperature) and $p_0 = 5\,\text{kPa}$ ($\approx 168\,\text{dB}$). Note that 40 kHz is chosen in this example as this is the most commonly used frequency in the literature[20].

From Fig. 1, when the normalized density of the particle is 10^2, the maximum ARF is achieved when the normalized radius is ≈ 0.2. However, as the particle density approaches the density of

air ($\rho_p/\rho_0 = 10^0$), regions of high ARF occur at $r_p/r_0 \approx 0.35$, 0.55 or 0.85. It is interesting to note that there are combinations of radius and density that do not produce any acoustic radiation force (the green lines in Fig. 1, also overlayed in Fig. 2 and 3 for reference).

The inertia of the particle is $F_{inert}(\rho_p, r, a) = -Ma$ where $M = M_p + M_f$, $M_p = \frac{4}{3}\pi r^3 \rho_p$ is the particle mass, and $M_f = \frac{2}{3}\pi r^3 \rho_0$ is the added mass[9]. The gravitational force is $F_{grav}(\rho_p, r) = -M_p g$ with $g = 9.81\,\mathrm{m\,s^{-2}}$, the buoyancy force is $F_{buoy} = \frac{4}{3}\pi r^3 \rho_0 g$. The viscous drag force is[21]: $F_{drag}(r, v) = -\frac{C_d}{2}\pi r^2 \rho_0 v^2$. The coefficient of drag (C_d) is evaluated using the formulation by Morrison[22] (see supplementary material) and is valid if $\mathrm{Re} < 10^6$ (Reynolds number, $\mathrm{Re} = \frac{2rv\rho_0}{\mu}$) which is true for cases presented here. Since the particle motion is assumed to be sinusoidal, the points of maximum velocity and acceleration are offset in phase by $\frac{\pi}{2}$. Thus, it is possible to isolate the dynamic equation into two parts: (i) the force equation that is limited by the maximum velocity (viscous drag force); (ii) the force equation that is limited by maximum acceleration (inertia). Therefore, the AVD can fail by reaching the limit of either (i) or (ii) (or by reaching both (i) and (ii) simultaneously). We note that despite the offset between maxima of the inertial and
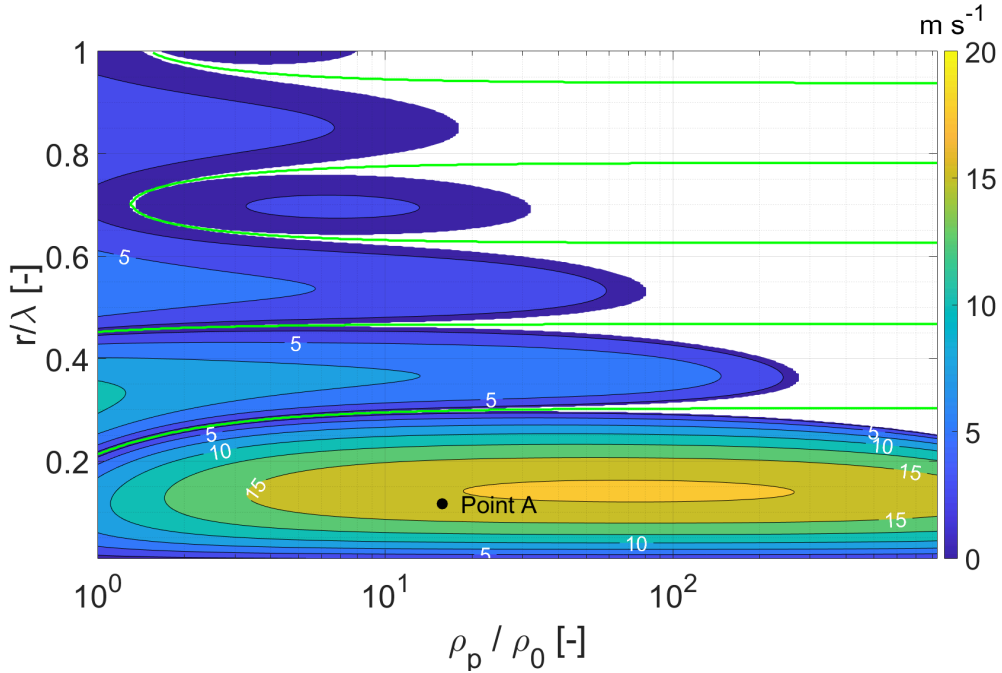

FIG. 2: Maximum achievable velocity v_{max}, given $f_f = 40\,\mathrm{kHz}$ and $p_0 = 5\,\mathrm{kPa}$. Empty regions in the figure represent invalid solutions i.e. $v_{max} < 0$, which can occur when the F_{grav} or F_{buoy} is greater than F_{rad}. The empty regions in Fig. 2 to 4 are similarly regions with invalid solutions. Green lines indicate zero ARF.

viscous forces, the total force (i.e. the sum of the inertial and viscous components) may be great than either of these two independent components. However, considering (i) and (ii) independently allows the limitations imposed by each force component to be determined independently. The small errors introduced by this assumption will be highlighted in relevant figures, and its effect is discussed in the supplementary material.

From Eq. 1 to 3; velocity amplitude is $v = A\omega_p$, and acceleration amplitude is a function of velocity $a = v\omega_p$. These identities are used to identify the performance limits of the AVD, and the maximum velocity limitation imposed by the viscous drag force is first evaluated using:

$$F_{rad}(\rho_p, r, f_f, p_0) + F_{gb}(\rho_0, \rho_p, r) + F_{drag}(r, v) = 0 \tag{4}$$

where $F_{gb}(\rho_0, \rho_p, r) = -|F_{grav}(\rho_p, r) + F_{buoy}(\rho_0, r)|$. For a given particle density (ρ_p), and radius of the particle (r); the maximum achievable velocity of the particle can be identified using the above equation. However, since Eq. 4 makes the function implicit, it is not possible to isolate the variable, v. Thus, a root-finding algorithm (Newton-Raphson) is utilized to determine the maximum achievable velocity, v_{max} (details in the supplementary material). The maximum achievable velocities are shown in Fig. 2, and the highest velocity ($17.8\,\mathrm{m\,s^{-1}}$) in Fig. 2 is achieved at a normalized radius and density of 0.141 and 70.2, respectively. Eq. 4 includes all dynamic effects; hence it is possible for the particle to move in the trajectory specified in Eq. 1 provided that sufficient ARF exists in the system. It is evident that the islands of contours in Fig. 2 are bounded by the green lines from Fig. 1 which indicates the zero acoustic radiation force. At the point of writing, the maximum particle manipulation velocity achieved in an acoustic levitator[4] is $8.75\,\mathrm{m\,s^{-1}}$ (acoustic radiation force amplitude $F_{rad} \approx 0.25\,\mathrm{mN}$, normalized particle radius ≈ 0.12, and particle density $= 19\,\mathrm{kg\,m^{-3}}$). This point corresponds to 'Point A' in Fig. 1 and 2, and the theoretical maximum achievable velocity (v_{max}), according to Fig. 2 is $17.0\,\mathrm{m\,s^{-1}}$ ($F_{rad} \approx 0.235\,\mathrm{mN}$). Thus, the maximum achievable velocity between the theoretical and experimental results differ by a factor of two. However, the maximum achievable velocity also depends on the trajectory of the path, and recent studies[3,18,19,23] have shown that the narrow bandwidth characteristics of acoustic transducers could limit the capability of the phased array to switch its phases effectively (and therefore displace the acoustic trap rapidly). It is interesting to note that neglecting the gravitational/buoyancy force in the formulation (equivalent to rastering in horizontal direction) does not significantly change the maximum velocity calculated in this manuscript (see supplementary material). This is due to the fact that, in most of the operating regions, the effect of gravity is small when compared to other
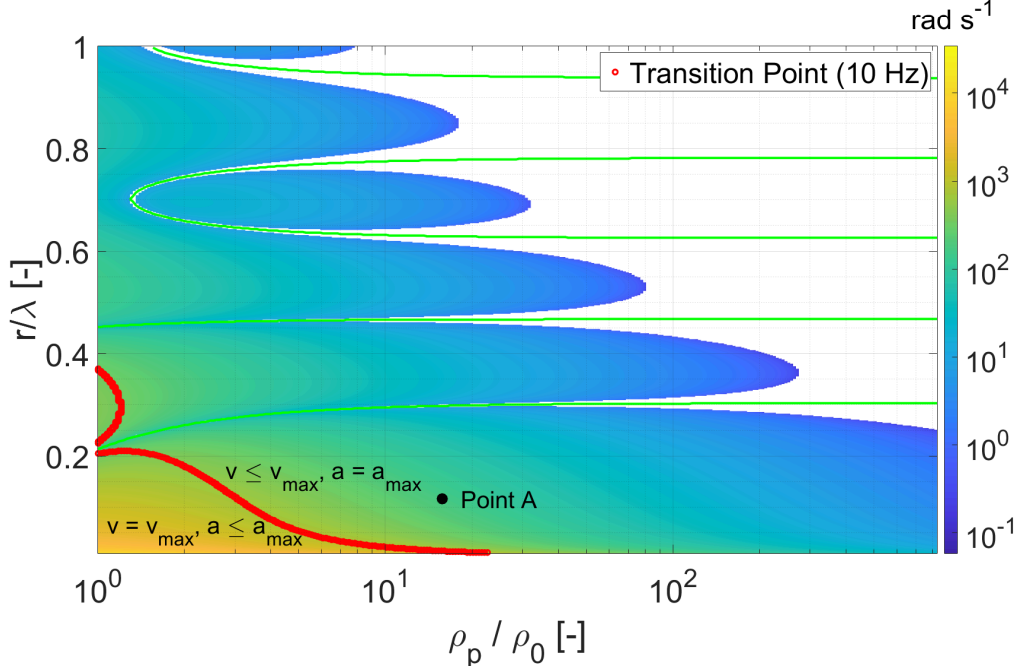
FIG. 3: Maximum achievable particle frequency ω_p^{max}, given $f_f = 40\,\text{kHz}$ and $p_0 = 5\,\text{kPa}$. The red line in the figure denotes the transition point between the regions limited by viscous drag or inertia, given $f_r = 10$ Hz. The green lines indicate zero ARF.

forces.

The performance limit imposed by the inertia of the particle is now evaluated, in order to define the maximum achievable acceleration. This limit is described by:

$$F_{rad}(\rho_p, r, f_f, p_0) + F_{gb}(\rho_0, \rho_p, r) + F_{inert}(\rho_p, r, a) = 0 \tag{5}$$

The frequency of the particle motion reaches its maximum when both the viscous drag force and the inertia forces are simultaneously at their maxima. The maximum acceleration (from Eq. 5) can then be used, along with the previously calculated maximum velocity (from Eq. 4) in the identity, $a = v\omega_p$, to find the maximum particle frequency (ω_p^{max}), given v_{max}: $\omega_p^{max} = \frac{1}{Mv_{max}}\left(F_{rad} - \left|\left(\frac{4}{3}\pi r^3 \rho_0 - M_p\right)g\right|\right)$.

The calculated particle frequency, ω_p^{max} is as shown in Fig. 3. The resultant maximum achievable particle frequency matches the intuition to minimize the radius and density for maximum acceleration. The physical meaning of this particle frequency, ω_p depends on the display mode, size and rendering frequency of the AVD. The reported maximum particle acceleration and frequency[3,4] are $141\,\text{m}\,\text{s}^{-2}$ and $578\,\text{rad}\,\text{s}^{-1}$, respectively, and the maximum acceleration and frequency at point A in Fig. 3 are $2850\,\text{m}\,\text{s}^{-2}$ and $168\,\text{rad}\,\text{s}^{-1}$, respectively.

7

In order to determine the maximum achievable size of the rendering area, some assumptions about the rendering method are required. Here we assume the AVD is a raster screen with 1:1 aspect ratio (similarly to that described by Fushimi et al.[3]), with screen constructed by packing the particles into the area of screen without any overlap. Thus the amplitude is $A = N_{par}r$ where N_{par} is the number of particles in one column of the render. The schematics and detailed derivations are available in the supplementary material. Following the derivation, the screen size (S_r) and particle frequency (ω_p^s) for 1:1 raster screen size are evaluated by $S_r = 2\sqrt{\frac{vr}{f_r\pi}}$ and $\omega_p^s = \sqrt{\frac{f_r\pi v}{r}}$, respectively.

By setting the limit of ω_p^s (when $v = v_{max}$) to ω_p^{max}; the transition point between the viscous drag and inertia limited region for a 1:1 raster screen can be evaluated and this is shown in Fig. 3. The red line line in Fig. 3 denotes this transition point when $f_r = 10\,\text{Hz}$ (the minimum rendering frequency required such that the graphics are visible to human eyes[24]). To the left of this red line, the performance of the AVD is limited by viscous forces (described by Eq. 4), and the maximum screen size can be evaluated by setting $v = v_{max}$ whilst ensuring $\omega_p^s \leq \omega_p^{max}$. To the right of the red curve, the region is limited by the inertia. Thus the acceleration $a = a_{max}$ (found from Eq. 5) needs to be achieved while $v \leq v_{max}$. For a 1:1 raster screen, this can be achieved by setting velocity $v_a = \left(\frac{(a_{max})^2 r}{f_r\pi}\right)^{\frac{1}{3}}$ and $\omega_p = \frac{a_{max}}{v_a}$.

The achievable screen size of 1:1 raster graphics, given rendering frequency ($f_r = 10\,\text{Hz}$) are as shown in Fig. 4. We note that the N_{par} is an integer number and the resultant screen size is discrete. However, for simplicity, we treat N_{par} as a continuous variable (see the supplementary material for details on the effects of discretizing N_{par}). The contour plot for $f_f = 40\,\text{kHz}$ and $p_0 = 5\,\text{kPa}$ shows that the maximum achievable screen size is 62.5 mm. Screen sizes above 60 mm are achieved by setting the normalized radius between 0.3-0.4, and normalized density up to ≈ 1.2. In the supplementary material, we explored cases where the particle density $\frac{\rho_p}{\rho_0} \leq 1$; however, we note that it is difficult to achieve this combination of particle density and boundary condition with current materials. Whilst this analysis has limited the particle to be rigid for simplicity: assigning finite compressional and shear wave speeds can generate higher ARF than a rigid assumption (an elastic assumption, using $c_c = c_s = 900\,\text{ms}^{-1}$ at point A results in 5.98 % difference between rigid and compressible particle assumptions, see supplementary material for details)[25].

Changing the acoustic frequency used in the AVD has an interesting effect on the performance, as demonstrated in Fig. 4. By reducing the acoustic frequency from 40 kHz to 20 kHz (whilst keeping constant acoustic pressure at 5 kPa), the maximum screen size increases from 62.5 mm
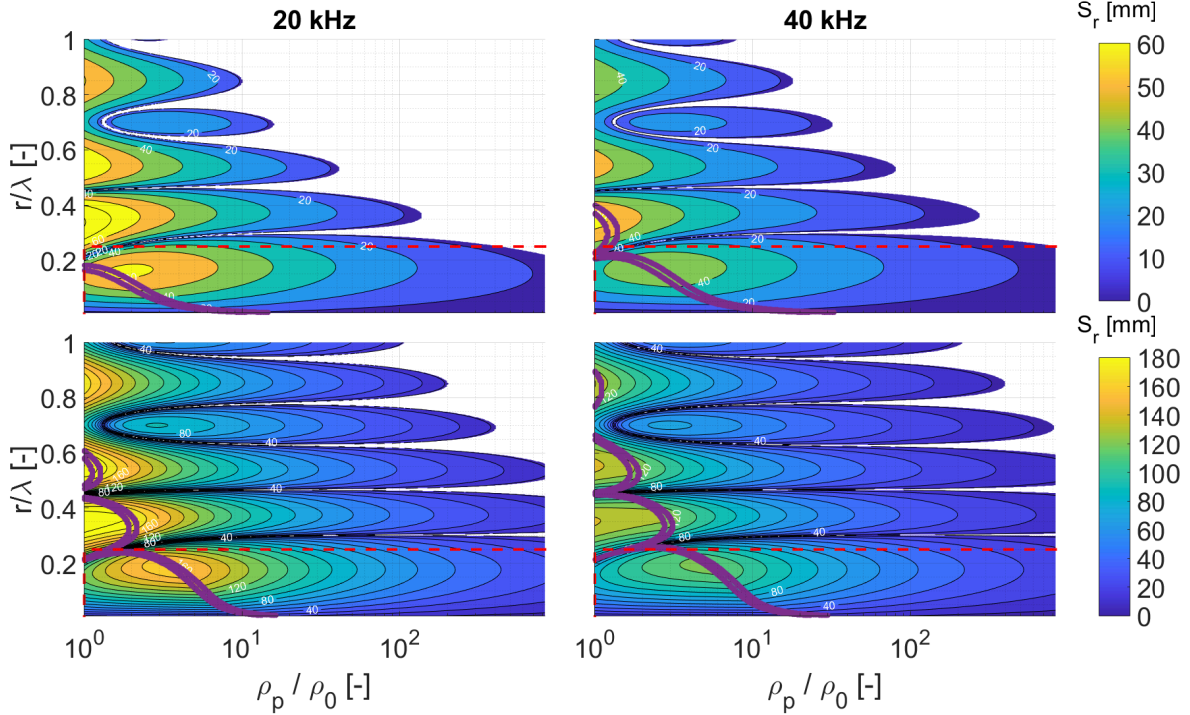
8

FIG. 4: Calculated screen size of 1:1 raster display given rendering frequency (f_r) of 10 Hz with acoustic frequency (f_f) of 20 and 40 kHz and acoustic pressure amplitude (p_0) of 5 and 25 kPa. The boundaries in purple indicate area where the total force exceeds 15% of the $max(F_{drag}, F_{inertia})$ (corresponding to an error in screen size between 3.77% and 10.4%, see supplementary material for detail). The red dashed box in the figure represents particles commonly used in acoustic levitation. Figure generated using tightplot[26]

at 40 kHz to 80.5 mm at 20 kHz (screen size can further be increased by reducing the acoustic frequency, but frequencies below 20 kHz are audible to humans observers[27]). This is in part due to the assumed raster scheme in which the particles are pixels which do not overlap. Hence at lower frequencies, the optimal particle size is larger and hence the size of the rendered object is larger.

A further increase in the screen size can be achieved by increasing the pressure amplitude of the acoustic field, which increases the amplitude of the acoustic radiation force applied to the particle. The improvements in the performance achieved by increasing the acoustic pressure amplitude from 5 kPa to 25 kPa are as shown in Fig. 4. By observing the shape of contour plot in Fig. 4, each graphical feature (e.g. presence of multiple islands, and empty regions) originates from limitations identified in each contour plot in Fig. 1 to 3. The envelope of the achievable screen size in Fig. 4 increases, and the maximum screen size increases to 200 and 142 mm in 20 and 40 kHz,

respectively. At the point of writing, one of the highest acoustic pressure amplitudes generated by a phased-array is by Inoue et al.[28] who generated 6 kPa using 1996 transducers at 40 kHz. The theoretical maximum acoustic pressure amplitude is 1 atmospheric pressure (101 kPa). Hence we produce results for a p_0 of 25 kPa which may be experimentally obtainable. However, we note that increasing the acoustic pressure amplitude further will result in additional nonlinear acoustic effects such as heating and field distortion[29], acoustic streaming[30,31], and thermoacoustic heating.

The red box ($\frac{\rho_p}{\rho_0} \geq 1$,$\frac{r}{\lambda} \leq 0.25$) in Fig. 4 indicates regions of commonly utilized particle size and density in acoustic levitation. The upper bound in normalized radius is based on the instability of ARF solution beyond this radius in a single-axis resonant levitator[32], and the lower bound of normalized density was approximated from Zang et al.[33] who levitated a soap bubble.

The results of a parametric study focusing on the red box in Fig. 4 are shown in Fig. 5. Here, the point of best performance, in terms of screen size, was selected as the optimum condition, and the evolution of the optima by increase in the pressure amplitude and acoustic frequency is studied. The screen size naturally increases with the pressure amplitude, and the optimum particle size is between a normalized radius of 0.16-0.2, which is near the ARF maxima in Fig. 1. It is interesting to observe that, whilst the increase in acoustic frequency decreases the achieved screen size, it increases the optimum particle density. Thus, if the material selection is limited, increasing the acoustic pressure could ease the achievement of a 1:1 raster display. In the supplementary material we present a study of the maximum achievable screen size and optimum particle radius with a commonly available expanded polystyrene particle[4] ($\rho_p = 19 \, \text{kg} \, \text{m}^{-3}$). Within the parameter space considered in Fig. 5, the maximum screen size of 117 mm is achieved at $f_f = 20$ kHz (minimum frequency) and $p_0 = 25$ kPa (maximum acoustic pressure) with a normalized particle radius of 0.175. For the majority of the parameter space considered, the maximum screen size is achieved at the transition point between the inertia and viscous force limited region. However, when the acoustic frequency and pressure are low (e.g. 20 kHz and below 8 kPa), the maximum performance is achieved in the inertia limited region (see supplementary material) and the optimal property remains constant. As the pressure amplitude increases, the maximum performance shifts towards the transition region, and the optimal condition begins to increase.

In this manuscript, the screen size of 1:1 raster graphics was chosen as the design parameter, but one can also utilize the screen resolution of the display (S_{pix}) as the design parameter (formulation is available in the supplementary material). The screen resolution can be maximized by increasing the acoustic frequency, with attenuation in the air providing an upper practical limit[34,35]. The
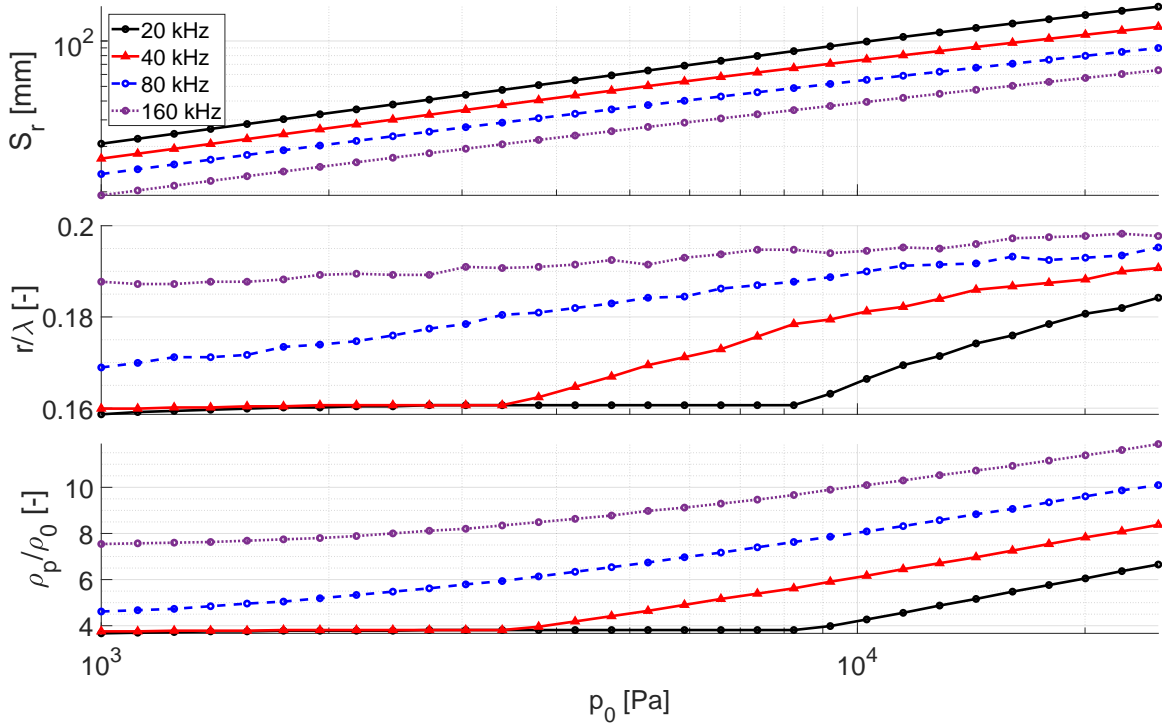
FIG. 5: Parametric study looking at the shift of maximum screen size condition in the red box in Fig. 4. The lower graphs show the corresponding particle size and density require to achieve the top maximum screen size plot.

current generation of AVDs and OTDs utilize a simple light source that emits light waves with a wide focus[1,3,4]. Thus, the particle size sets the rendering resolution; however, one can use alternative schemes. For example, the utilization of projection mapping[36] or active tracking lasers with tighter focal spots could render high-resolution graphics on the surface of particles. The analysis presented here is generic and similar methods can be applied to other AVD display formats (e.g. vector graphics) to identify the maximum theoretical performance or be utilized in trajectory planning and optimization. For some 3D displays (e.g. spherical or cylindrical displays), the surface can be unwrapped to 2D, and therefore the analysis presented here may be used. However, for some 3D displays with more complex topology, additional information regarding the rastering path would be required.

Whilst this study has limited the number of the particles utilized in AVD to one particle, simultaneous levitation of multiple particles has been demonstrated by various authors[4,37]. However, the force generated decreased with the number of particles as the acoustic intensity produced by the devices were shared across the particles. In addition, it is important to note, that even when the

11

number of particles in the AVD is increased, each particle is still limited by the same fundamental forces.

In conclusion, the generalized performance indices for an AVD were determined from the first principles, and the limits imposed by the fundamental forces (e.g. ARF, inertia, viscous damping) were explored. As the research into AVDs is beginning to bloom, the design approach shown here will provide insight into the future AVD designs by demonstrating methods for identifying the maximum theoretical performance, and steps necessary to achieve a high performing AVDs in the coming years.

See supplementary material for the details on the comparison of acoustic radiation force evaluation, drag coefficient equation, Newton-Raphson setup, description of 1:1 raster display, introduced inaccuracy, and case studies.

The data that supports the findings of this study are available within this article and its supplementary material. The program codes are openly available in Zenodo at [URL].

REFERENCES

[1] D. E. Smalley, E. Nygaard, K. Squire, J. Van Wagoner, J. Rasmussen, S. Gneiting, K. Qaderi, J. Goodsell, W. Rogers, M. Lindsey, K. Costner, A. Monk, M. Pearson, B. Haymore, and J. Peatross, Nature **553**, 486 (2018).

[2] J. Berthelot and N. Bonod, Optics Letters **44**, 1476 (2019), arXiv:1806.06662.

[3] T. Fushimi, A. Marzo, B. W. Drinkwater, and T. L. Hill, Applied Physics Letters **115**, 064101 (2019).

[4] R. Hirayama, D. Martinez Plasencia, N. Masuda, and S. Subramanian, Nature **575**, 320 (2019).

[5] C. R. P. Courtney, C. E. M. Demore, H. Wu, A. Grinenko, P. D. Wilcox, S. Cochran, and B. W. Drinkwater, Applied Physics Letters **104**, 1 (2014).

[6] K. Melde, A. G. Mark, T. Qiu, and P. Fischer, Nature **537**, 518 (2016).

[7] M. A. B. Andrade, A. L. Bernassau, and J. C. Adamowski, Applied Physics Letters **109**, 044101 (2016).

[8] T. Fushimi, T. L. Hill, A. Marzo, and B. W. Drinkwater, Applied Physics Letters **113**, 034102 (2018).

[9]K. McKee and A. Czarnecki, American Journal of Physics **87**, 165 (2019).

[10]L. P. Gor'kov, Soviet Physics Doklady **6**, 773 (1962).

[11]T. Hasegawa and K. Yosioka, The Journal of the Acoustical Society of America **46**, 1139 (1969).

[12]L. Zhang and P. L. Marston, The Journal of the Acoustical Society of America **129**, 1679 (2011).

[13]P. Glynne-Jones, P. P. Mishra, R. J. Boltryk, and M. Hill, The Journal of the Acoustical Society of America **133**, 1885 (2013).

[14]H. Bruus, Lab on a Chip **12**, 1014 (2012).

[15]O. A. Sapozhnikov and M. R. Bailey, The Journal of the Acoustical Society of America **133**, 661 (2013).

[16]X. Chen and R. E. Apfel, The Journal of the Acoustical Society of America **99**, 713 (1996).

[17]M. Caleap and B. W. Drinkwater, Proceedings of the National Academy of Sciences of the United States of America **111**, 6226 (2014).

[18]L. Cox, A. Croxford, B. W. Drinkwater, and A. Marzo, Applied Physics Letters **113** (2018), 10.1063/1.5042518.

[19]A. Marzo, M. Caleap, and B. W. Drinkwater, Physical Review Letters **120**, 44301 (2018).

[20]R. H. Morris, E. R. Dye, P. Docker, and M. I. Newton, **101301** (2019), 10.1063/1.5117335.

[21]J. Ward-Smith, *Mechanics of Fluids, Ninth Edition* (CRC Press, 2012).

[22]F. A. Morrison, "Data correlation for drag coefficient for sphere," (2013).

[23]S. Suzuki, M. Fujiwara, Y. Makino, and H. Shinoda, IEEE Transactions on Haptics , 1 (2020).

[24]R. W. Bowen, J. Pola, and L. Matin, Vision Research **14**, 295 (1974).

[25]T. Hasegawa, Journal of the Acoustical Society of America **65**, 32 (1979).

[26]P. Kumpulainen, "tight_subplot(Nh, Nw, gap, marg_h, marg_w)," (2020).

[27]A. Rodríguez Valiente, A. Trinidad, J. R. García Berrocal, C. Górriz, and R. Ramírez Camacho, International Journal of Audiology **53**, 531 (2014).

[28]S. Inoue, S. Mogami, T. Ichiyama, A. Noda, Y. Makino, and H. Shinoda, The Journal of the Acoustical Society of America **145**, 328 (2019).

[29]M. A. B. Andrade, N. Pérez, and J. C. Adamowski, The Journal of the Acoustical Society of America **136**, 1518 (2014).

[30]S. J. Lighthill, Journal of Sound and Vibration **61**, 391 (1978).

[31]J. Lei, M. Hill, and P. Glynne-Jones, Lab on a Chip **14**, 532 (2014).

[32]R. R. Whymark, Ultrasonics **13**, 251 (1975).

[33]D. Zang, K. Lin, L. Li, Z. Chen, X. Li, and X. Geng, Applied Physics Letters **110**, 121602

(2017).

[34] H. E. Bass, L. C. Sutherland, A. J. Zuckerwar, D. T. Blackstock, and D. M. Hester, Journal of the Acoustical Society of America **97**, 680 (1995).

[35] M. A. Abdelaziz and D. G. Grier, Physical Review Research **2**, 013172 (2020), arXiv:1910.03670.

[36] T. Sueishi, H. Oku, and M. Ishikawa, 2015 IEEE Virtual Reality Conference, VR 2015 - Proceedings , 97 (2015).

[37] A. Marzo and B. W. Drinkwater, Proceedings of the National Academy of Sciences **116**, 84 (2018).